



## ISTITUTO NAZIONALE DI RICERCA METROLOGICA Repository Istituzionale

Paramagnetic defects in polycrystalline zirconia: An EPR and DFT study

This is the author's accepted version of the contribution published as:

*Original*

Paramagnetic defects in polycrystalline zirconia: An EPR and DFT study / Gionco, C.; Paganini, M. C.; Giamello, E.; Burgess, R.; Di Valentin, C.; Pacchioni, G.. - In: CHEMISTRY OF MATERIALS. - ISSN 0897-4756. - 25:11(2013), pp. 2243-2253. [10.1021/cm400728j]

*Availability:*

This version is available at: 11696/66290 since: 2021-02-01T14:58:47Z

*Publisher:*

AMER CHEMICAL SOC

*Published*

DOI:10.1021/cm400728j

*Terms of use:*

This article is made available under terms and conditions as specified in the corresponding bibliographic description in the repository

*Publisher copyright*

American Chemical Society (ACS)

Copyright © American Chemical Society after peer review and after technical editing by the publisher. To access the final edited and published work see the DOI above.

(Article begins on next page)

# Paramagnetic defects in polycrystalline zirconia: an EPR and DFT study

Chiara Gionco<sup>a</sup>, Maria Cristina Paganini<sup>a</sup>, Elio Giamello<sup>\*a</sup>, Robertson Burgess<sup>b</sup>, Cristiana Di Valentin<sup>b</sup>, Gianfranco Pacchioni<sup>b</sup>

<sup>a</sup>Dipartimento di Chimica, Università di Torino and NIS, Nanostructured Interfaces and Surfaces Centre of Excellence, Via P. Giuria 7, I - 10125 Torino, Italy

<sup>b</sup>Dipartimento di Scienza dei Materiali, Università di Milano-Bicocca, Via R. Cozzi, 53, 20125, Milano, Italy

**KEYWORDS.** Zirconium Oxide, defects, EPR, DFT.

---

**ABSTRACT:** The paramagnetic defects present in pristine zirconium dioxide and those formed upon reductive treatments (either annealing or UV irradiation in H<sub>2</sub>) are described and rationalized by the joint use of Electron Paramagnetic Resonance (EPR) and DFT supercell calculations. Three types of Zr<sup>3+</sup> reduced sites have been examined both in the bulk of the solid (one centre) and at the surface (two centres). Trapping electron centers different from reduced Zr ions are also present, whose concentration increases upon annealing. A fraction of these sites are paramagnetic showing a symmetric signal at  $g = 2.0023$  but the majority of them are EPR silent and are revealed by analysis of electron transfer from the reduced solid to oxygen. The presence of classic F type centres (electrons in bulk oxygen vacancies) is disregarded on the basis of the  $g$  tensor symmetry. This is expected, on the basis of theoretical calculations, to be anisotropic and thus incompatible with the observed signal. The hypothesis of the presence of electron trapping sites in line defects and grain boundaries of the polycrystalline solid, supported by recent work on other oxides, is advanced. In general terms zirconium dioxide has some properties similar to typical reducible oxides such as TiO<sub>2</sub> and CeO<sub>2</sub> (excess electrons stabilized at cationic sites) but is much more resistant to reduction than this class of materials. While point defects in doped (Y<sup>3+</sup>, Ca<sup>2+</sup>) zirconium dioxide materials have been widely investigated for their role as ionic conductors, the defectivity of pristine ZrO<sub>2</sub> is much less known and this paper presents a thorough analysis of this phenomenon.

---

## 1. INTRODUCTION

Zirconium dioxide is an important material for technological applications. It has a high melting point and exists in three main polymorphs (cubic, tetragonal and monoclinic). The cubic phase has a fluorite structure while the other two phases derive from progressive distortions of the cubic one. The monoclinic polymorph is stable at low temperature but has scarce applications in ceramic technologies due to cracking during the tetragonal to monoclinic transition, the latter having larger volume and a very anisotropic thermal expansion. At variance, the two polymorphs stable at high and intermediate temperature (cubic and tetragonal respectively) have excellent mechanical, thermal and dielectric properties which make zirconium dioxide an excellent candidate to prepare protective coatings, high-k dielectric materials, chemically inert refractory materials and other objects<sup>1</sup>.

Important applications, widely used in technology, are those involving Y- or Ca-doped zirconium dioxide. The wide miscibility of zirconia with lower valence metal oxides ( $\text{Y}_2\text{O}_3$ ,  $\text{CaO}$ ) stabilizes the cubic phase containing compensative oxygen vacancies which make it an excellent ionic conductor with application in electrochemical oxygen sensors and in solid oxide fuel cells (SOFC)<sup>2</sup>. Zirconium dioxide is also an important material in heterogeneous catalysis and, to a lesser extent, in heterogeneous photocatalysis.

Due to the thermal stability and the presence of both surface acid and basic sites,  $\text{ZrO}_2$  has found applications in a series of catalytic reactions including hydrogenation, dehydration and skeletal isomerization of hydrocarbons<sup>3-5</sup>. The interest in  $\text{ZrO}_2$  for photocatalysis is limited by both the large band gap energy (around 5 eV) and the weak activity in photooxidation. However, the high negative value of the conduction band edge represents an advantage in terms of reductive potential. For this reason  $\text{ZrO}_2$  has been tested in water photosplitting for hydrogen production<sup>6</sup> and in the photoactivation of carbon dioxide<sup>7,8</sup>.

Despite the importance of  $\text{ZrO}_2$  as a multi-functional advanced material and in catalytic and photocatalytic reactions, the surface science and the defectivity of this oxide are less known, in general, than those of other oxides. Actually, the systems containing oxygen vacancies because of extrinsic defectivity (cubic Y-doped and Ca-doped  $\text{ZrO}_2$ <sup>9, 10</sup>) and the epitaxially growth ultra-thin films<sup>11</sup> have been studied in some detail for their practical applications, while the defectivity of the tetragonal and monoclinic polymorphs is not yet fully explored. This is particularly true in the case of nanosized materials which are usually rich of structural imperfections and defects deriving from their preparation route. Years ago, preliminary activity of some of us put into evidence an apparent anomaly in the behavior of polycrystalline monoclinic zirconia, i.e. the presence of partially reduced centres (essentially  $\text{Zr}^{3+}$ ) at the surface of the solid treated

in oxygen at high temperature<sup>12, 13</sup>. Furthermore, annealing under vacuum was shown to induce electron transfer from the solid to gaseous oxygen to form surface adsorbed superoxide ions, without the involvement of  $\text{Zr}^{3+}$  reduced centers<sup>14</sup>. In other words, vacuum activated zirconia seems to behave as a reservoir of hidden, EPR invisible, electrons which can be transferred to adsorbed acceptors ( $\text{O}_2$ ). Data confirming the presence of reduced centers in activated zirconia were reported later by other authors<sup>15</sup> but a thorough analysis of the features of defective zirconia is still lacking.

In the present paper the problem of the defectivity of undoped tetragonal and monoclinic polycrystalline  $\text{ZrO}_2$ , together with its behavior upon reduction and subsequent reoxidation, is revisited combining state of the art theoretical calculations with new experiments on two kinds of samples, the former constituted by a practically pure monoclinic phase, the latter having primarily (80%) tetragonal phase. This composition reflects the difficulties in preparing pure phases of the low temperature polymorphs maintaining an acceptably small particle size and an adequate surface extension. This hurdle is however only apparent as the behavior of the two phases (whose structures are not so different from each other) in the spectroscopic experiments reported in the following is strictly similar. For this reason the data reported in the following concern the tetragonal phase (theory) and the sample which is primarily of tetragonal phase (experiments).

## 2. EXPERIMENTAL AND COMPUTATIONAL DETAILS

### 2.1 Experimental details

All reactants employed in this work were purchased by Aldrich and used without any further purification treatment. Double distilled water was used in the synthesis procedures.  $\text{ZrO}_2$  samples were prepared following the sol-gel route described by Livraghi et al<sup>16</sup>. A solution containing zirconium propoxide, 2-propanol (with alkoxide/alcohol molar ratio 1:4) and water (alcohol/water ratio 1:2) was prepared stirring continuously at room temperature. The gel formed was aged over night, then dried in an oven at 50°C. The xerogel was then divided into two batches. The former was calcined in air at 773K for 2 hours, the other one was calcined at 1273K for 48 hours.

Prior to spectroscopic characterization the samples of the calcined oxide were activated, to remove surface impurities generated by contact with the atmosphere, by annealing in dynamic vacuum at 773K followed by a treatment of one hour in oxygen atmosphere at the same temperature.

### 2.2 Characterization

Powder X-rays diffraction (XRD) patterns were recorded with a PANalytical PW3040/60 X'Pert PRO MPD using a copper  $K\alpha$  radiation source (0.15418 nm) and a X'Pert High-Score software for data handling. Rietveld

refinement was performed on the diffraction patterns to determine the crystallite size and relative abundance of phases, using the MAUD 2.26 software and a NIST Si powder to determine the instrumental function.

UV-Vis absorption spectra were recorded using a Varian Cary 5 spectrometer, coupled with an integration sphere for diffuse reflectance studies, using a Carywin-UV/scan software. A sample of PTFE with 100% reflectance was used as reference.

EPR spectra recorded at room temperature and at liquid nitrogen temperature (77K) were run on a X-band CW-EPR Bruker EMX spectrometer equipped with a cylindrical cavity operating at 100 kHz field modulation. The effect of light on EPR spectra was investigated using a 1000 W mercury/Xenon lamp (Oriel Instruments) equipped with a IR water filter.

### 2.3 DFT calculations

Density functional theory calculations were performed under a linear combination of atomic orbitals (LCAO) approach, using the CRYSTAL09 package<sup>17,18</sup>. Exchange and correlation terms were calculated with the B3LYP hybrid functional<sup>19,20</sup>. The O atoms were modeled using an 8-411(d) Gaussian-type basis set. A [Kr] 311G31d basis set and a Hay and Wadt small core effective core potential (ECP) were used for the Zr atoms. Only the 4s and 4p electrons were defined outside of the pseudopotential. Calculations of systems with odd numbers of electrons were performed using a spin polarized approach. The reciprocal space is sampled using a regular sublattice with a shrinking factor of 2, and the condition for convergence of the SCF cycle was set to  $10^{-6}$  a.u.

Calculations were performed on a 108 atom supercell, corresponding to  $3 \times 3 \times 2$  unit cells of the  $\text{ZrO}_2$  tetragonal phase. The optimal lattice parameters for the non-defective system compare well with the experimental values (see below). Oxygen vacancies were calculated with 4 different charges, from -1 to +2. The basis set corresponding to the removed oxygen atom was left in the vacancy, forming a site for ghost functions. A neutral vacancy was calculated by removing an oxygen nucleus, as well as eight electrons from that site. That left 2 electrons still allocated to the vacancy site (F center, see below). Vacancies with charges of +1 and +2 were generated by further removing 1 and 2 electrons from the vacancy site. A vacancy with a formal charge of -1 was generated by returning one electron to the neutral vacancy site.  $\text{Zr}^{3+}$  defects were also investigated. This was done by simply adding an extra electron to the neutral model. The calculation of charged systems under periodic boundary conditions requires the addition of a background charge to ensure that the total system is neutral.

All systems underwent a geometry relaxation calculation, using a Broyden-Fletcher-Goldfarb-Shanno

scheme. Both atom locations and cell parameters were allowed to change under the geometry relaxations, and symmetry restraints were also removed. The convergence criteria was set to an RMS of the gradient of  $3 \times 10^{-4}$  a.u. and an RMS of the maximum atomic displacement of  $1.2 \times 10^{-3}$  a.u. and the convergence criteria of the maximum gradient and atomic displacement was set to 1.5 times their respective RMS criteria.

Transition energy levels were calculated using the method already outlined in previous publications<sup>21</sup>. Using this method, the vertical or optical transition energy from a state of charge  $q$  to a state of charge  $q'$  (where  $q'$  is always  $q + 1e^-$ ) can be calculated using the following formula:

$$\varepsilon(q/q') = E_{q'} - E_q = [eq(N) + eq'(N+1)]/2 \quad (1)$$

where  $eq'(N+1)$  is the energy of the highest occupied crystal state of the system of charge  $q'$ , and  $eq(N)$  is the energy of the lowest unoccupied crystal state of the system of charge  $q$ , with both energies referenced to the top of the valence band which is set as the zero energy level.

## 3. Results

### 3.1 X-Ray diffraction

X-ray diffraction analysis was performed to identify the nature of the crystalline phases present in the samples after synthesis. The diffraction patterns of the two  $\text{ZrO}_2$  samples (Z773 and Z1273 respectively) are shown in Figure 1. In the case of Z773 the peaks are broad due to the small size of the crystallites while for Z1273 the narrow peaks are due to the relatively large crystal size produced by high temperature sintering. The tetragonal (T) and the monoclinic (M) polymorphs of  $\text{ZrO}_2$  are both present in Z773 (Fig. 1).

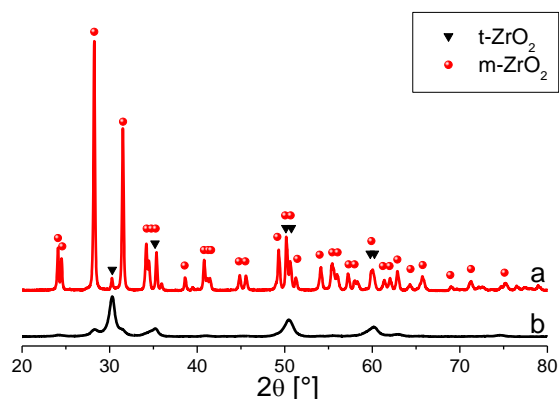


Figure 1. XRD patterns of (a) Z1273 and (b) Z773.

On the XRD patterns a Rietveld refinement was performed using the MAUD software<sup>22</sup>. The tetragonal phase is more abundant in Z773 (the T/M ratio is about 80:20) while the material calcined at high temperature

(Z1273) is constituted essentially by monoclinic zirconia (98%) with some 2% of the tetragonal phase.

### 3.2. Diffuse Reflectance UV-Vis Spectroscopy (DR-UV-Vis)

The optical spectra of the two materials (mainly tetragonal, Z773 and monoclinic, Z1273) exhibit relatively small differences one from the other and confirm previous data reported in the literature<sup>23</sup>. The two spectra are dominated by the valence band (VB) – conduction band (CB) transition occurring at about 250 nm (ca. 5 eV). The two spectra are only distinguished by a small difference in the slope of the VB → CB transition.

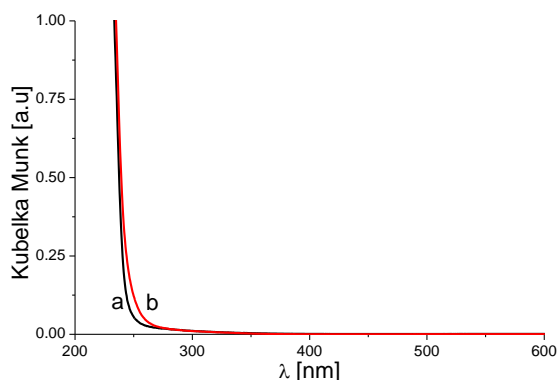


Figure 2. Absorption spectra of Z773 sample a) as prepared and b) reduced in vacuo 6h at 600°C.

Fig. 2 compares the optical absorptions of a Z773 sample recorded after preparation (line 2a) and after annealing in vacuo at 873K for 6 hours (line 2b). There is practically no difference between the two spectra except for small additional absorption shown by the reduced sample close to the band gap transition.

Two main points show up from UV-Vis spectroscopy. First, the optical properties of the tetragonal and monoclinic phases are very similar. Second, the solid is quite resistant to reduction since a prolonged annealing at high temperature (Fig. 2b) causes tiny modifications only of the whole absorption. This means that zirconium dioxide is very different from more reducible oxides like titanium dioxide or cerium dioxide which, in the same conditions, lose oxygen altering their optical properties both in the visible and in the NIR region, due to the abundant formation of excess electrons.

### 3.3. Redox behaviour and paramagnetic defects investigated via EPR Spectroscopy

Since many kinds of point defects present in solids, and in particular in oxides, are paramagnetic, Electron Paramagnetic Resonance (EPR) spectroscopy is one of the

most suitable techniques to investigate defective materials. As it will be shown in this section, the behavior of the two materials here examined is basically the same also in the case of EPR analysis (except for the spectra intensity, which is always slightly lower in the case of the highly sintered Z1273 material), indicating that the nature and properties of defects are substantially the same, at least for the tetragonal and the monoclinic polymorphs of  $\text{ZrO}_2$ . The EPR spectrum of bare zirconia, recorded after the final calcination in air, is not a flat line (as one should expect in the case of the perfect stoichiometry) and shows two distinct weak signals, indicating the presence of some intrinsic defects in the as prepared material. The signals monitored in this experiment are reported, in Fig. 3. The first one (Fig. 3, spectrum a) is an axial signal with  $g_{||}=1.9768$  and  $g_{\perp}=1.9589$  (signal I) already reported in the literature and assigned to  $\text{Zr}^{3+}$  sites<sup>12, 14, 16, 24-27</sup>. A second symmetric and even weaker signal is present, resonating at  $g=2.0024$ , i.e. the free electron value (signal II). In a series of independently prepared samples we have found a certain variability of signals I and II intensities and, in some cases, the intensity of the second one is at the limit of detectability.

The reductive treatment of bare  $\text{ZrO}_2$  was performed under vacuum at 873K for 1 hour.

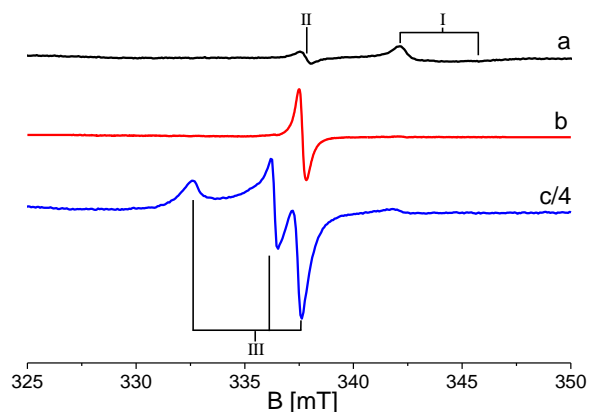
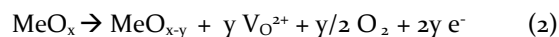


Figure 3. EPR spectra of Z773 at two different magnifications. a) as prepared sample after activation, b) after reduction by annealing in vacuo at 873K, c) after contact with oxygen at 400K. All spectra have been recorded at 77K.

This kind of treatment, in the case of reducible oxides, induces the loss of oxygen and generates, beside oxygen vacancies ( $\text{V}_{\text{O}^{2+}}$ ) various types of reduced species or even conduction electrons<sup>28</sup>

For a generic oxide ( $\text{MeO}_x$ ) one has:



The effect of the annealing treatment under vacuum is apparently paradoxical in that signal I disappears, while

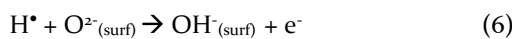
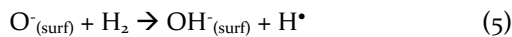
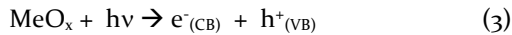


signal II **grows** in intensity (Fig. 3, spectra a and b). The effective oxygen loss during annealing is demonstrated by the fact that contacting the annealed solid with gaseous oxygen at room temperature the EPR spectrum changes, roughly recovering the initial background spectrum (signals I and II) and producing a new signal (III) at lower field, unambiguously assigned to superoxide  $O_2^-$  ions adsorbed at the surface on  $Zr^{4+}$  ones<sup>12, 13, 29</sup>. An electron transfer thus occurs between the reduced solid and the adsorbed molecule. The intensity of signal III further increases if the sample is heated in oxygen at about 400K indicating that the electron transfer is somehow activated. The spectrum of adsorbed superoxide after this further increment is reported in Fig. 3c, its intensity is about five times higher than that of the spectrum of Fig. 3b. The intensity of this signal can be reasonably assumed as a measure of the whole excess electrons in the solid and thus, indirectly, of the oxygen loss upon annealing. Its value is, however, definitely smaller by about one order of magnitude than those recorded in the same conditions for other semiconducting oxides ( $TiO_2$ ,  $CeO_2$ ),<sup>27</sup> indicating for zirconia intermediate properties between true reducible oxides and non-reducible systems like alkaline earth oxides. The g tensor of the superoxide in Fig 3c is the same reported by some of us<sup>13</sup> with  $g_{zz}=2.0336$ ,  $g_{yy}=2.0096$ ,  $g_{xx}=2.0034$ . In parallel with the formation of superoxide, the signal present in the background shows up again roughly recovering the initial intensity. This is particularly visible for the signal I ( $Zr^{3+}$ ) which is not overlapped with that of superoxide ions. The spectra in Fig. 3c demonstrate three important facts:

an oxygen loss with parallel reduction of the solid actually occurs upon annealing at 873K even if to a relatively small extent

the majority of the electrons generated by reduction escape EPR detection (Fig. 3b) and is likely associated to diamagnetic states (vide infra).

To further investigate the redox behavior of  $ZrO_2$ , a fully oxidized sample of the oxide has been UV irradiated employing a 1000 W lamp in  $H_2$  atmosphere to produce reactive H atoms. In such conditions the holes generated in the valence band by the UV induced charge separation migrate at the surface where they interact with molecular hydrogen. The homolytic splitting<sup>30-32</sup> of  $H_2$  generates reactive hydrogen which eventually reacts at the surface injecting electrons into the solid:



The fate of the electrons generated by the described photochemical process (3-6) depends on the nature of the oxide. In the case of insulating oxides (alkaline-earth oxides for instance) the electrons are trapped at single ion or multi-ion positive centres at the surface, generating the so-called "surface colour centres"<sup>33</sup>. In the case of

semiconducting oxides the electrons are injected into the solid with formation of reduced centers (for instance,  $Ti^{3+}$  ions are formed in  $TiO_2$ )<sup>32-36</sup>.

The results in the case of Zirconia ( $ZrO_2$ ) are shown in Fig. 4 and Fig. 5, obtained by irradiating in  $H_2$  i) a fully oxidized material (see Fig. 3a) and ii) an annealed one (see Fig. 3b), respectively. The two parallel experiments were scheduled because of the different situation of the two starting materials. Signal I ( $Zr^{3+}$ ) in fact dominates the oxidized sample (Fig. 3a and 4a) while signal II dominates the vacuum annealed one (Fig. 3b and 5a). The irradiation in  $H_2$  of the oxidized zirconia markedly modifies the spectral region of signal I. The modification (Fig. 4b) can be described in terms of the overlap of signal I with two new broader signals (IV and V) having axial structure and slightly different g values. The two new signals have the same perpendicular g value ( $g_{\perp}=1.978$ ) and differ in the parallel component only (Table 1, simulation in Fig. 4b'). The species corresponding to signal IV and V are, together, one order of magnitude more intense than those corresponding to signal I. The features of this spectrum allow us to assign also species IV and V to  $Zr^{3+}$  ions having different coordinative environment from those corresponding to species I.

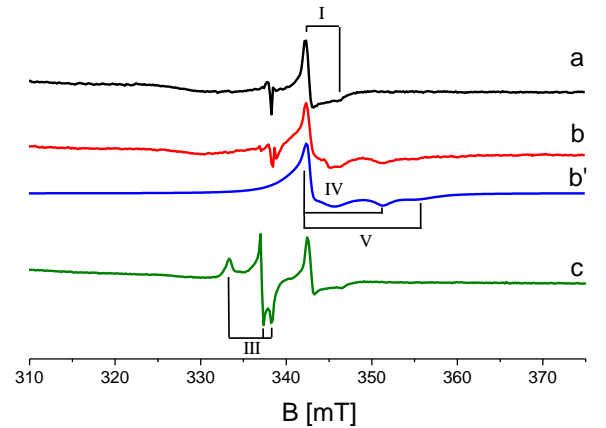


Figure 4. EPR spectra of  $ZrO_2$  a) as prepared sample after oxidative activation, b) after UV irradiation in  $H_2$ , b') computer simulation of b), c) adsorption of  $O_2$  at room temperature. All spectra have been recorded at 77K.

The broad line width of species IV indicates a certain degree of heterogeneity (several species slightly different in spectral parameters) typical of disordered environments, such as those found at the surface of nanostructured crystals. Even broader signals are found, for instance, for species formed at the surface of  $TiO_2$ <sup>32</sup>. Adsorbing oxygen at room temperature on the irradiated sample the formation of superoxide is again observed at the expense of the new signals IV and V which completely vanish leaving the only signal I unaffected, at its the

original intensity (compare 4c with 4a). The formation of superoxide is, in this case, complete at room temperature. This corresponds to a non activated electron transfer confirming the surface nature of the involved  $Zr^{3+}$  ions (species IV and V). The g values of this superoxide species are the same of that in Fig. 3c indicating that the adsorption site is the same in the two cases. The second experiment (Fig. 5) performed on the partially reduced system (Signal II dominates the background, Fig. 5a) has the same result as the previous one, with formation of species IV and V. The signals of these two species are now observed (Fig. 5b) without interference with the signal of species I.

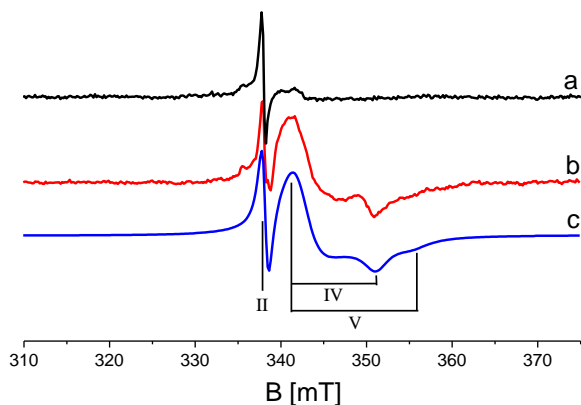


Figure 5. EPR spectra of Zr773 a) as prepared sample after reduction, b) reduced sample after UV irradiation in  $H_2$ , c) computer simulation of b). All spectra have been recorded at 77K.

The effect of the interaction with atomic hydrogen seems to be the same for the two types of samples (fully oxidized and vacuum annealed). This, interestingly, suggests that the surface of zirconia crystals is not much affected by the annealing treatment. Remarkably the zirconium dioxide sample which does not adsorb visible light after calcination nor after prolonged annealing (Fig. 2) becomes pale grey-violet after treatment in atomic hydrogen. This indicates that the energy of the surface  $Zr^{3+}$  centers (signal IV and V) is separated from the conduction band by an energy corresponding to a visible frequency (see Section 3.5 DFT calculations).

To summarize, the interaction with photo-generated hydrogen atoms leads to a pair of previously unreported  $Zr^{3+}$  species which are due to ions located in the disordered environment of the surface. With respect to the injection of electrons at the surface (reaction with  $H$ ),  $ZrO_2$  is thus more similar, in qualitative terms, to the reducible oxides (e.g.  $TiO_2$ ) rather than to the non-reducible alkali-earth oxides since the excess electrons are stabilized in d orbitals of the metal ions and not on surface morphological defects.<sup>33</sup> However the intensity of

the EPR spectra of adsorbed superoxide ions recorded in various experiments of annealing under vacuum (which roughly corresponds to the amount of electrons trapped in the reduced material) indicates that  $ZrO_2$  is, with respect to other reducible oxides such as  $TiO_2$  or  $CeO_2$ , more reluctant to loose oxygen.

### 3.4 Features and stability of electron excess centres

In the previous section we have identified four different EPR signals (respectively species I, II IV and V) corresponding to paramagnetic defects in  $ZrO_2$ . Two of them are visible, though with very low intensity, in the oxidized starting material indicating that the oxide is not easy to obtain in a fully oxidized stoichiometry.

The nature of the three species is resumed in Table 1 and discussed in the following. Species I, IV and V resonate in the spectral region expected for a  $d^1$  configuration ( $Zr^{3+}$  is a  $4d^1$  ion) showing, in the X band, an apparently axial EPR signal. In the fluoritic structure of zirconium dioxide, the positive  $Zr^{4+}$  ions are eight-coordinated by oxygen anions. However, both tetragonal and cubic polymorphs undergo a quite strong distortion with respect to the perfect cubic phase. For this reason an axial symmetry of the  $Zr^{3+}$  cationic centre is reasonable and it cannot be excluded that, recording the spectra at very high frequencies, a lower symmetry (rhombic) of the signal could be put into evidence. The assignment of species I, IV and V to  $Zr^{3+}$  centres in axial symmetry is therefore unambiguous. Although very few reports on  $Zr^{3+}$  are available in the literature, the more investigated  $Ti^{3+}$  with analogous configuration ( $3d^1$ ) and axial symmetry exhibits similar g values<sup>16, 32, 37, 38</sup>.

Species I, already present in the starting material (Fig. 3a), disappears upon reductive annealing (Fig. 3b) probably due to the formation of more stable defects and reappears after a partial reoxidation of the material (Fig. 3c). This very species also forms (Figure 6) when  $ZrO_2$  is UV irradiated in vacuo at 77K.

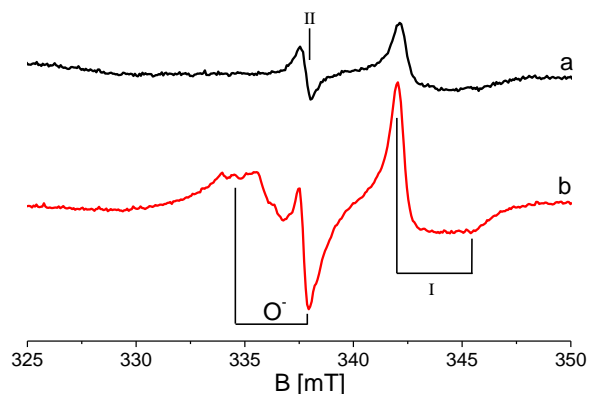


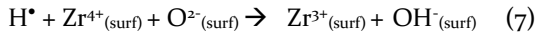
Figure 6. EPR spectra of  $ZrO_2$  a) as prepared sample, b) after UV irradiation in vacuo at 77K. All spectra have been recorded at 77K.

In this case the intensity of species I in the background becomes about twice the original one and in parallel a signal due to trapped holes ( $O_{(surf)}^-$ , see equations 2 and 3) shows up. Heating the system at room temperature after irradiation, electrons and holes quickly recombine, recovering the initial situation. This experiment demonstrates that species I indeed corresponds to an electron trapping center. A strict parallel exists between this behaviour and that of  $TiO_2$  for which the charge separation experiment leads to a  $Ti^{3+} - O^-$  pair<sup>39</sup>. As mentioned above,  $Ti^{3+}$  in this case is a bulk species corresponding to a “regular” Ti site of the lattice with  $g_{||}=1.99$  and  $g_{\perp}=1.97$ , very close to those monitored here for species I. We thus assign this centre to bulk  $Zr^{3+}$  ions in the structure of tetragonal zirconia (see below the discussion of DFT results).

**Table 1. g-factor and assignments for species I to V.**

Species	$g_{xx}$	$g_{yy}$	$g_{zz}$	Assignment
I	1.9768		1.9589	Bulk $Zr^{3+}$
II	2.0024			Symmetric trapping site
III	2.0025	2.0096	2.033	Surface adsorbed superoxide ion $O_2^-$
IV	1.9784		1.9288	Surface $Zr^{3+}$
V	1.9784		1.9060	Surface $Zr^{3+}$

The features of the spectrum resulting from irradiation in hydrogen allow us to assign species IV and V to  $Zr^{3+}$  ions having different coordinative environment from those corresponding to species I. Their g tensor differs from that of species I in particular for the  $g_{||}$  value which is clearly lower ( $g_{||}=1.928$  and  $1.906$ ). The relatively large linewidth of these two species indicates a certain degree of heterogeneity (several species with slightly different spectral parameters) typical of disordered environments such as those found at the surface of nanostructured crystals. Species IV and V are assigned to surface reduced  $Zr^{3+}$  species formed upon H atoms ionization which is a process indeed occurring at the surface:



The quick and non activated reaction of these species with oxygen (Fig. 5c) reinforces the assignment.

Species II has a symmetric EPR spectrum whose g value coincides with the free spin value. The hypothesis of the presence of surface carbon radicals due to cracking of organic molecules (which accidentally have similar features) is discarded as the signal is insensitive to oxidation at high temperature and increases its intensity upon oxygen depletion by annealing (Fig. 4a and 4b). A possible assignment for species II would be that of an electron trapped in an oxygen vacancy (corresponding to

F centres in alkaline-earth oxides; here we use the same notation). A neutral F centre (two electrons associated to the vacancy created by the removal of a neutral O atom,  $V_O$ ) is diamagnetic while a single electron centre ( $F^+$ , or  $V_O^+$ ) is paramagnetic and in alkaline-earth oxides has a symmetric g tensor due to the spherical symmetry, in that case, of its wavefunction. The nature of the site corresponding to signal II remains elusive and will be discussed below in connection with DFT calculations.

The presence of other, EPR invisible, defect centres has to be considered, however, on the basis of the results reported in Fig. 3. The intensity of the superoxide signal III (Fig. 3c) is in fact by far higher than that of the electron centres in Fig. 3b. In other words, the number of electrons scavenged at the surface by the acceptor oxygen molecule is larger (more than 5 times) than that monitored by EPR of paramagnetic centres in the reduced material (Fig. 3b). This indicates that the majority of electrons trapped in the solid after oxygen depletion are non visible in EPR and likely trapped in diamagnetic centres (See Section 4). The abundance of these sites is thus significant. In ionic oxides (alkaline-earth oxides) paramagnetic  $F^+$  centres are usually accompanied by two-electrons diamagnetic ones (F). However, recent studies show that the presence of classical F and  $F^+$  centers (O vacancies) in pristine alkaline-earth oxides is very low due to their high formation energy<sup>33, 40</sup>.

A second reductive channel consists in the interaction of the solid with photogenerated H atoms (UV irradiation in  $H_2$ ). In this case excess electrons are stabilized by  $Zr^{4+}$  ions probably located at the surface of the solid since the EPR signal of the corresponding  $Zr^{3+}$  species differs from signal I, which is assigned to bulk  $Zr^{3+}$  species. The absence of signal II due to oxygen depletion is due to the fact that in the condition of the treatment ( $H_2$  reactivity at low temperature) no oxygen is released from the sample.

In the following the nature of electron trapping sites in  $ZrO_2$  is discussed based on DFT supercell calculations and the proposed assignments are compared to the theoretical outcomes.

### 3.5 DFT calculations

In this section we present the results from DFT calculations of defect centers potentially present in  $ZrO_2$ . The aim is to provide tentative assignments of the features observed in EPR measurements. Unfortunately, no direct observable quantity can be compared with theory. In fact the key parameters of an EPR spectrum are the g-tensor and the hyperfine coupling constants. These latter, in particular, provide important information on the spin distribution. Hyperfine coupling constants could not be obtained from the experimental spectra due to the low natural abundance of Zr atoms with non-zero nuclear spin. These quantities could be derived from spin



polarized DFT calculations using all electron basis sets on the atoms of interest. Here we made use of a pseudopotential to represent the core electrons of the Zr atoms in order to reduce the computational cost. Therefore, hyperfine coupling constants are not accessible on either side, theory and experiment. Different is the case of g-tensor. This is the key quantity to assign the features in the experimental EPR spectra. However, the calculation of g-tensors is a delicate issue and requires the use of cluster models to represent a given defect. Attempts to compute g-tensors for paramagnetic defects in  $\text{ZrO}_2$  have been reported in the literature but with only partial success<sup>41</sup>. This may be related to the intrinsic problems connected with the calculation of g-tensors or with the use of cluster models. On the other hand, an important information coming from EPR spectra is the symmetry of the g tensor which reflects the symmetry of the paramagnetic site. Therefore, the following discussion is largely based on the ground state geometry and symmetry of defects, the spin distribution and the position of the associated states in the gap of  $\text{ZrO}_2$ . This latter aspect is related to the optical properties of each defect, another point of contact with experimental measurements.

Before to discuss the results on the point defects, we briefly address the electronic structure of bulk  $\text{ZrO}_2$ . Pure tetragonal zirconia has a  $P4_2/nmc$  space group and was calculated to have cell parameters of  $a=3.6055 \text{ \AA}$  and  $c=5.1797 \text{ \AA}$ , in reasonable agreement with other calculations and experimental results<sup>23</sup>. Each O atom has two nearest neighbor Zr atoms at a distance of  $2.06 \text{ \AA}$ , and two next-nearest neighbor Zr atoms at a distance of  $2.40 \text{ \AA}$ , with these four atoms being arranged in a distorted tetrahedral arrangement around the O atom, Fig. 7. For the rest of this paper these Zr atoms shall be labelled 1, 2 (nearest neighbor) and 3 and 4 (next nearest neighbor). The distance between atoms 1 and 2 and atoms 3 and 4 are  $3.61 \text{ \AA}$ , whereas the distance from either of atoms 1 and 2 to either of atoms 3 or 4 is  $3.63 \text{ \AA}$ .

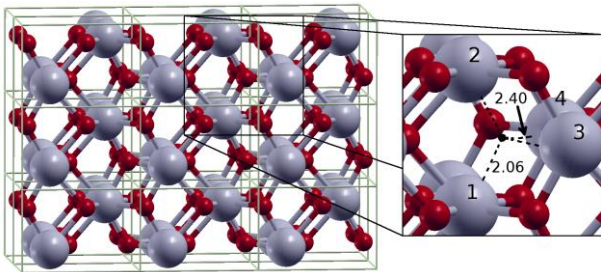


Figure 7. Structure of tetragonal zirconia. Zr: large blue spheres, O: small red spheres. Inset: An oxygen atom has been removed, the vacancy site being a center for basis set functions, with the neighboring atoms labeled. Distances are in Angstroms

The band structure and the density of states (DOS) of the system are given in Figure 8. It should be

noted that they were plotted over a larger range of energies in the case of the bulk material than for the defective systems. With the B3LYP functional the band-gap at the  $\Gamma$  point is approximately  $5.8 \text{ eV}$ . This is higher than the measured bandgap of  $4.2 \text{ eV}$  using electron energy loss spectroscopy (EELS)<sup>42</sup> but within the range measured using vacuum-ultraviolet (VUV) absorption spectroscopy ( $5.78\text{-}6.62 \text{ eV}$ )<sup>23</sup>. The calculated dispersion of the VB is quite low, whereas there is dispersion of almost  $1 \text{ eV}$  in the low-energy edge of the CB. The right hand panel of Figure 8 shows that, not surprisingly, the DOS of the VB is dominated by the O  $2p$  states, and the CB by the Zr  $4d$  states.

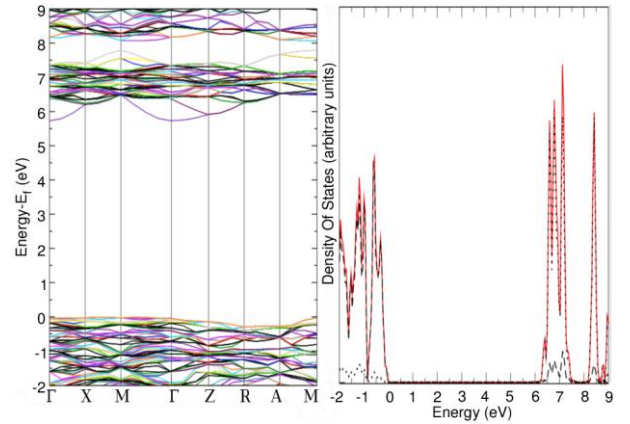


Figure 8. Calculated band structure (left) for bulk tetragonal  $\text{ZrO}_2$ . Right: Density of states for bulk tetragonal  $\text{ZrO}_2$ . The total DOS is given in red, the DOS projected onto the zirconium d states is given by the dashed line, whilst the DOS projected onto the oxygen sp states is given by the dotted line. The zero of energy has been set to the highest occupied level (top of the valence band).

### 3.5.1 Nature of $\text{Zr}^{3+}$ species

We start by considering the paramagnetic  $\text{Zr}^{3+}$  species. Calculations on this system starting from the bulk atomic arrangement caused the charge of the extra electron to become delocalised and distribute across the supercell. To prevent this unphysical result, the oxygen atoms were moved radially away from the  $\text{Zr}^{3+}$  site approximately  $0.2 \text{ \AA}$  in order to account for the polaronic distortion accompanying the formation of the reduced Zr ion. After relaxation of the system, we obtain a lower energy solution where the four nearest neighbor O atoms are all located  $2.18 \text{ \AA}$  (maximum deviation  $0.0002 \text{ \AA}$ ) away from the  $\text{Zr}^{3+}$  site, compared to the bulk distances of  $2.06 \text{ \AA}$  and  $2.40 \text{ \AA}$ . These four O atoms, as in the bulk case, are arranged in a distorted tetrahedral arrangement, grouping the O atoms into two pairs. Each oxygen atom has an  $\text{O-Zr}^{3+}\text{-O}$  bond angle with its partner of  $117.4^\circ$  and bond angles of  $105.7^\circ$  with the other two oxygen atoms. This distortion is similar to that for the bulk case,

however there the bond angles are  $122.0^\circ$  and  $103.6^\circ$ , respectively and the distances are equal in pairs. The arrangement of O atoms around this defect site has  $D_{2d}$  symmetry, which is fully consistent with the assignment of the axial signal with  $g_{||}=1.9768$  and  $g_{\perp}=1.9589$  to the  $Zr^{3+}$  defect.

After geometry relaxation the extra electron stayed localised to the zirconia atom, in a defect state approximately 0.5 eV below the bottom of the CB, Fig. 8. Thus, the corresponding energy level is high in the gap. Figure 9 reports also the total spin density of the system, showing that the unpaired electron is localised around a Zr 4d orbital. The situation is reminiscent of that of lattice  $Ti^{3+}$  ions in bulk  $TiO_2$  which also give rise to localized 3d levels just below the CB<sup>43</sup>.

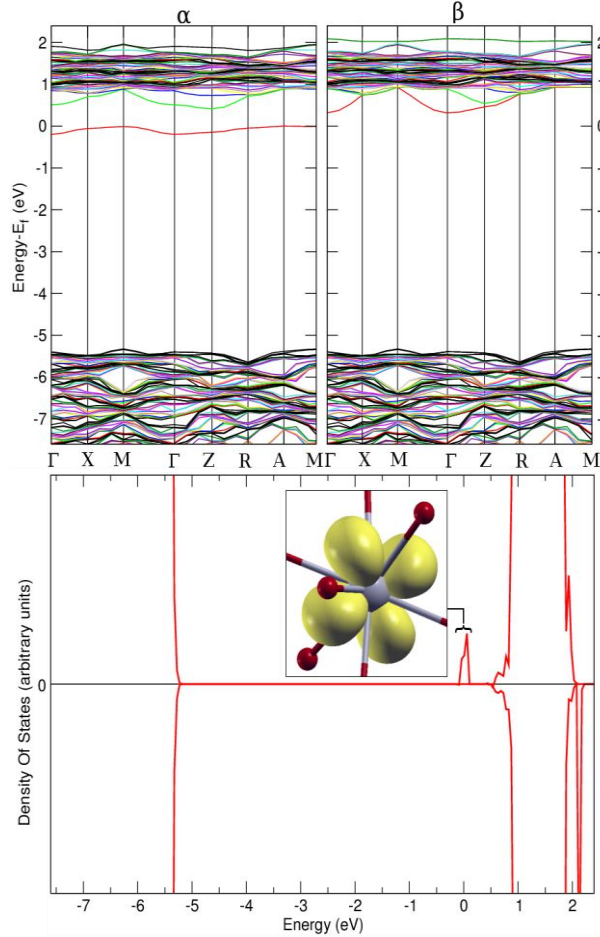


Figure 9. Band structure (top) and density of states (bottom) of the system with one zirconia atom with an extra electron. Positive density of states indicates spin-up states and negative density of states indicates spin-down states. Inset: An isosurface of the electron density projected onto the occupied defect state. The zero of energy has been set to the highest occupied level.

### 3.5.2 Nature of the neutral oxygen vacancy $V_O$ (F center)

We have seen above that some evidence exists of diamagnetic electron traps in  $ZrO_2$ . A potential candidate

for these traps is the O vacancy,  $V_O$ . After geometry relaxations the total formation energy of this defect was calculated to be 7.2 eV relative to  $1/2 O_2$ . This formation energy is similar to that of a neutral F center in MgO (about 7 eV)<sup>44, 45</sup> and much larger than that of the same defect in  $TiO_2$  ( $\sim 4$  eV) or  $CeO_2$ <sup>46</sup>, thus confirming the non-reducible nature of  $ZrO_2$ . The high formation energy of an O vacancy suggests that the number of these defects in thermodynamic equilibrium should not be too high.

Structural rearrangements are restricted to the atoms immediately surrounding the vacancy site, as for neutral  $V_O$  centers in MgO. The nearest neighbor Zr atoms move radially from the vacancy site. Atoms 1 and 2 move towards the site  $\sim 0.12$  Å to a distance of  $\sim 1.94$  Å and atoms 3 and 4 move away from the site  $\sim 0.16$  Å to a distance of 2.56 Å from the center. This movement results in the distance between atoms 1 and 2 being 3.47 Å whilst atoms 3 and 4 movement away from the vacancy gives a 3  $\rightarrow$  4 interatomic distance of 3.71 Å. These structural variations cause negligible change to the distance between the pairs, with the relaxed distance being 3.65 Å. A summary of the distances between the zirconia atoms around an oxygen vacancy at a different charge state is given in Table 2.

Table 2 - Unit cell size and distances between zirconia atoms of bulk  $ZrO_2$  and systems with oxygen vacancies. 1  $\rightarrow$  2 indicates the distance between zirconia atoms 1 and 2, whilst 1,2  $\rightarrow$  3 indicates the distance between either atoms 1 or 2, and atom 3. All distances are in Angstroms.

	Cell parameter a	1 $\rightarrow$ 2	3 $\rightarrow$ 4	1,2 $\rightarrow$ 3	1,2 $\rightarrow$ 4
O4C	3.61	3.61	3.61	3.63	3.63
VOo	3.64	3.47	3.71	3.65	3.65
VO+	3.75	3.94	3.83	3.66	3.71
VO2+	3.91	4.70	4.061	4.47	4.47
VO-	3.54	3.20	3.57	3.41	3.41

The removal of an O atom creates a doubly-occupied defect energy level within the bandgap, approximately 3.3 eV above the VB, Figure 10. Figure 10 also shows the DOS of the system around the Fermi level and, in the inset, an isosurface of the electron density projected onto this defect state. The state is highly localised at the vacancy site with some density on the zirconium atoms 1 and 2. In this respect, it closely resembles a neutral  $V_O$  center in alkaline-earth oxides, and has the typical structure of an F center<sup>47</sup>.

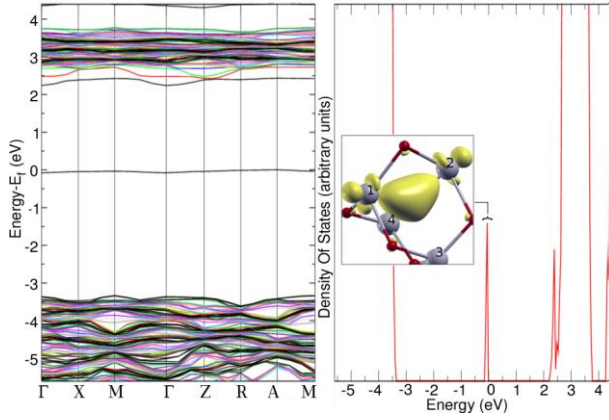


Figure 10. Band structure (left) and density of states (right) for the system with a neutral oxygen vacancy ( $V_O$ ). Inset: An iso-level of the electron density projected onto the defect state. The zero of energy has been set to the highest occupied level.

### 3.5.3 Nature of the positively charged oxygen vacancies $V_O^+$ and $V_O^{2+}$ ( $F^+$ and $F^{2+}$ centers)

Removing one electron from the neutral  $V_O$  leads to the  $V_O^+$  defect. The corresponding electronic state splits into two spin-separated components. This results in a singly-occupied spin-up state, which, as in the case of the neutral O vacancy, is approximately 3.3 eV above the VB. A spin-down unoccupied defect state is also formed, just below the CB, Fig 11.

The inset in Figure 11 shows an isolevel of the electron density projected onto the occupied defect state. The state is localised to the vacancy site similarly to the neutral case, but now also encompasses atom 3 in a three-center arrangement. A Mulliken population analysis of the spin of the system shows that 33% of the spin is located at the vacancy, whereas 20, 20 and 15% of the spin is located at each of the Zr atoms 1, 2 and 3, respectively. However, Mulliken charges are strongly basis set dependent and should be taken with great care. The spin density plot shows quite unambiguously that the unpaired electron is located in the vacancy, typical of  $F^+$  centers in alkaline-earth oxides<sup>47</sup>.

The geometry relaxations are significantly different to the neutral case. Zr atoms 1 and 2 move apart from each other approximately 0.3 Å such that the distance between them becomes 3.94 Å. Atom 4 moves away from the vacancy center such that its new interatomic distances are 3.83 Å from atom 3 and 3.71 Å from atoms 1 and 2. The distance between atom 3 and atoms 1 and 2 remains almost unchanged, at 3.66 Å, Table 2. The most important conclusion from this analysis is that the relaxation leads to a strong asymmetric site where the electron is trapped. A reduction of symmetry around the  $V_O^+$  site was also shown by previous calculations on O vacancies in the monoclinic structure<sup>48</sup>. Around the  $V_O^+$  site atoms relax

in a distorted two-pair arrangement similar to that of the bulk tetragonal  $ZrO_2$ . The reduction of symmetry calculated for the  $V_O^+$  center is inconsistent with the experimentally measured highly symmetric isotropic signal with  $g = 2.0024$ . This, together with the high formation energy of O vacancies, casts some doubts about the possible assignment of the trapping site identified in the experiments to these specific defects.

Removal of the electron from  $V_O^+$  (formation of  $V_O^{2+}$  site) results in no defect states in the bandgap but in new states at the bottom of the CB. The O atoms around the vacancy move significantly away from the vacancy site, atoms 1 and 2 to a distance of 2.71 Å and atoms 3 and 4 to a distance of 2.76 Å. This gives the distances between the atomic pairs 1 and 2, 3 and 4 of 4.70 Å and 4.06 Å respectively, and the distance between two atoms of opposing pairs is 4.47 Å. As for  $V_O^{2+}$  centers in MgO, the abundance of these sites in the as-prepared material is expected to be extremely low as the formation energy is very high implying to add to the cost of removing a neutral O atom also the cost of the double ionization of the  $V_O$  center.

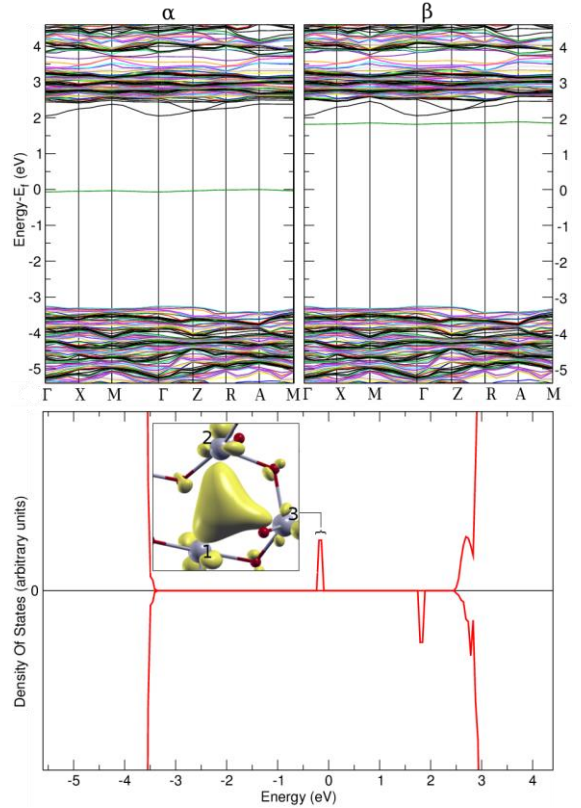


Figure 11. Band structure (top) and density of states (bottom) of the system with a single oxygen vacancy and a formal charge of +1. Positive density of states indicates spin-up states and negative density of states indicates spin-down states. Inset: An iso-level of the electron density projected onto the occupied defect state. The zero of energy has been



set to the highest occupied level.

### 3.5.4 Nature of the negatively charged oxygen vacancy $V_O^-$ ( $F^-$ center)

It has been suggested that neutral  $V_O$  centers in  $ZrO_2$  can also trap one electron to form another type of paramagnetic center<sup>21</sup>. We considered this defect simply by adding an extra electron to the neutral  $V_O$  center. As a consequence of the different number of up and down spins, the double-occupied defect state splits into two spin-resolved states, with an energy separation of about 0.1 eV. These two states are slightly lower than the defect state for the neutral O vacancy, at approximately 3.0 eV above the VB. A third, singly-occupied, spin-up defect state is about 1.5 eV above the other defect states, making it about 4.5 eV above the VB, Figure 12.

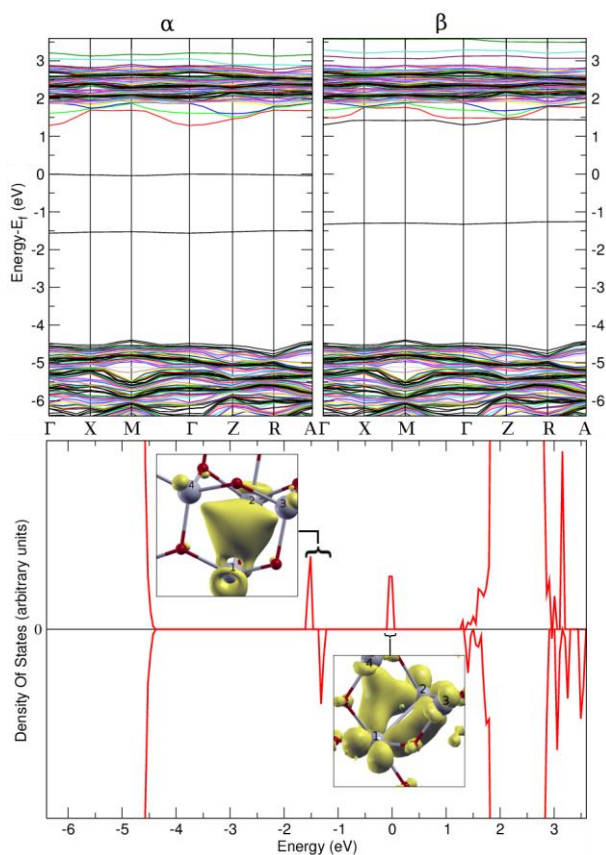


Figure 12. Band structure (top) and density of states (bottom) of the system with a single oxygen vacancy and a formal charge of -1. Positive density of states indicates spin-up states and negative density of states indicates spin-down states. Insets: Isolevels of the electron density projected onto the occupied defect states. The zero of energy has been set to the highest occupied level.

Insets in Figure 12 show the isosurfaces of the charge density for the pair of states associated to the  $V^-$  center.

The lower two states are similar to the doubly occupied state of the neutral  $V_O$  center and is mostly localized to the vacancy site, with some contribution from the neighboring Zr atoms, particularly atoms 1 and 2. The highest defect state, by contrast, is quite different. As can be seen this state involves mostly the 4d levels of the Zr ions around the vacancy site. Two 4d orbitals form a  $\pi$  bond between the atoms 1 and 2, while a  $\sigma$  bond is formed from atom 3 for one component, and atom 4 for the other component.

In this case all four atoms move towards the site. The interatomic distances are 3.20 Å between atoms 1 and 2 and 3.57 Å between atoms 3 and 4. The distance between either of the closer zirconia atoms to either of the further zirconia atoms is 3.41 Å. Since the interatomic distances between atoms 1 and 2, and atoms 3 and 4 are no longer equal, this breaks the  $D_{2d}$  symmetry around the vacancy. As such, this defect is also not consistent with the symmetric isotropic signal with  $g=2.0024$ .

### 3.5.5 Transition levels for point defects in $ZrO_2$

A more rigorous description of the position of the defect states in the band gap and a direct comparison with experimental spectroscopic data require to go beyond the single particle approximation (Kohn-Sham eigenvalues) and to compute transition energy levels. To this end we used a recently developed approach<sup>21</sup>, where total energy differences between different charge states ( $V_O^{-1,0,+1,+2}$ ) are approximated on the basis of Janak's theorem from single particles eigenvalues. Optical transition levels ( $\epsilon^{opt}$ ) can be directly compared with the position of the defect levels estimated from optical excitation, Fig. 13.

Oxygen vacancies create a series of transition levels 3.5-3.8 eV above the VB. These transitions are well above the visible light threshold. On the other hand, an optical absorption edge at around 2 eV is expected for reduced zirconia (oxygen vacancies), as electrons could be excited from the  $V_O$  states into the bulk CB. This should correspond to a change in the color of the sample as function of the level of O removal and chemical reduction, an effect that has not been observed in the procedures described above.

The transition energy for transferring an electron from the VB into the  $Zr^{3+}$  defect state is substantially higher, at around 5.6 eV. This indicates that the optical absorption edge for exciting an electron from the VB into the CB for pure zirconia would be around 5.6 eV. Conversely, if  $Zr^{3+}$  defects were introduced, likely through the addition of impurities, then the absorption edge for exciting these defect state electrons into the CB would be well below 1 eV, in the infra-red region of the absorption spectrum. Notice that the  $Zr^{3+}$  centers created at the surface of the oxide by reaction with atomic hydrogen, see reaction (6), could lead to deeper energy levels due to the stabilizing effect of a proton adsorbed in the vicinity.

In summary, the theoretical analysis of the

optical properties of  $V_O$  centers in various charge states suggests that some coloring effect should be present in connection to the appearance of these centers, at variance with experimental evidence. On the contrary, the gap states introduced by bulk  $Zr^{3+}$  species are not expected to give rise to any absorption in the visible, while this may be possible for the same centers formed at the surface of the oxide.

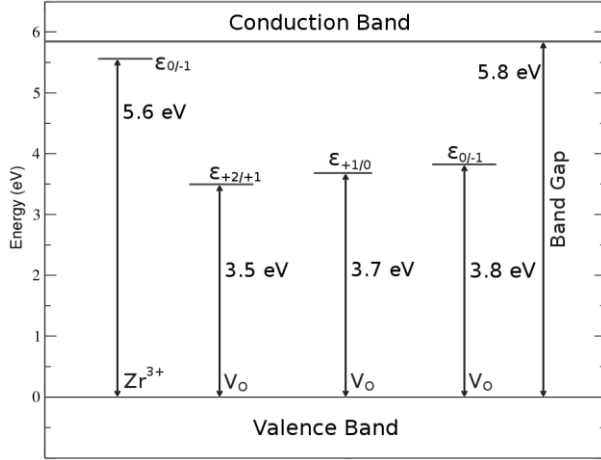


Figure 13. Summary of the optical transition energy levels for  $Zr^{3+}$  and  $V_O^{-1,0,+1,+2}$  defect centers from DFT B3LYP calculations.

#### 4. Discussion and conclusions

We have studied with EPR measurements and DFT hybrid functional calculations the nature of paramagnetic defects in  $ZrO_2$  powders prepared via sol-gel. The EPR spectrum of bare  $ZrO_2$  after calcinations in air shows two distinct signals indicating the presence of some intrinsic defects in the as prepared material. Species I corresponds to an axial signal with  $g_{||}=1.9768$  and  $g_{\perp}=1.9589$  already reported in the literature and assigned to  $Zr^{3+}$  sites. Species II are much less abundant, their origin is less obvious and will be discussed below.

The zirconia samples have been chemically reduced by following two different methods, either involving or not involving oxygen depletion. In the first case, reduction is obtained via annealing at high temperature. Oxygen is removed from the sample and the associated electrons are stabilized in both diamagnetic and paramagnetic sites (signal II in EPR spectra). Diamagnetic centers (not detectable by EPR) are more abundant as shown by the formation of an intense spectrum of superoxide ions via electron transfer from the solid to adsorbed  $O_2$  molecules (Fig. 3). The activated nature of this electron transfer (Fig. 3) suggests that the electrons associated to reduced centres are not simply located at the surface. Remarkably,  $Zr^{3+}$  centres (signal I) which are unstable in the reduced solid (cfr. Fig. 3a and 3b) are formed again after

reoxidation (Fig. 3c). The presence of a weak amount of  $Zr^{3+}$  in the starting material after oxidative treatment can be explained as the result of the presence in the solid of traces of some aliovalent impurity bearing one extra electron (e.g Nb, Ta). In such a case, similarly to what happens in Nb doped  $TiO_2$ <sup>27</sup>, one possible response of the system to the perturbation is the localisation of the extra electron on a lattice cationic sites ( $Zr^{4+} \rightarrow Zr^{3+}$ ). The formation of new and more stable trapping centers upon annealing (Fig. 3b,c) scavenges the extra electrons causing the temporary disappearance of signal I which forms again upon recovery by reoxidation of the initial situation.

The second reduction channel consists in the adsorption of photogenerated H atoms. In this case (Fig. 4) excess electrons are stabilized by Zr ions located at the surface of the solid since the EPR signal of the corresponding  $Zr^{3+}$  species differs from signal I, which is assigned to bulk  $Zr^{3+}$  species. The absence, in Fig. 4, of signal II associated to O depletion is due to the fact that in the conditions of the treatment ( $H_2$  reactivity at low temperature) no oxygen is released from the sample.

The results of the DFT calculations allow us to confirm some assignments and to discard others. First of all, if a proper polaronic distortion of the  $ZrO_2$  lattice is allowed, the calculations show that indeed a lattice Zr ion can trap one electron fully localized into a 4d orbital. This paramagnetic centre has a corresponding energy level just below the conduction band. The symmetry of the site is fully consistent with the axial character of the g-tensor, reinforcing the assignment of signal I to bulk centres in  $ZrO_2$  (Table I).

Signals IV and V have been assigned to surface  $Zr^{3+}$  ions whose electronic state is deeper in the band gap with respect to the bulk species I. This effect is understood in terms of the additional stabilisation provided by the nearby hydroxyl group (see equation 7) in parallel to what already found by DFT calculations on the  $(Ti^{3+}-OH)_{surf}$  group at the surface of titania<sup>43</sup>.

Much more problematic is the identification of the origin of the second signal (species II). We have considered various charge states of an O vacancy (F center), but several arguments lead us to conclude that these sites cannot be related to the observed features in EPR and optical spectra. First of all, a neutral  $V_O$  defect has a very high formation energy, similar to that of other wide gap insulators like MgO. The high formation energy is not consistent with the abundance of these defects at thermodynamic equilibrium. In this work we have considered only bulk  $V_O$  defects, and lower formation energies are expected on the surface of the material. However, a strong argument against the assignment of the paramagnetic species II to  $V_O^+$  (one electron removed) or  $V_O^-$  (one electron added) species lies in the symmetry of the site. The EPR spectra clearly show that the environment of the trapped electron must be highly symmetric. On the contrary, the optimal geometry of  $V_O^+$



and  $V_O^-$  centers is highly distorted and inconsistent with the isotropic EPR signal. We have considered only bulk defects, but the symmetry of the site can only be lower on the surface of the material. The third argument against  $V_O$  defects is that they should give rise to optical transitions in the visible region, and that the samples should be coloured as a consequence of their formation. This is not what is observed, and is another reason to discard the  $V_O^+$  or  $V_O^-$  centers as the sites responsible for the signal II.

Another important experimental observation is the reactivity of the unknown diamagnetic electron traps (X centers) with electron acceptors like  $O_2$  to give rise to superoxide anions and new paramagnetic defects:



This reaction implies that (a) the diamagnetic X center has occupied levels higher than the  $O_2 \pi^*$  accepting orbitals, and (b) that it is close to the surface or that its electrons can easily be transferred to the  $O_2$  species adsorbed on the surface. While bulk  $V_O$  defects fulfil the first requirement (the doubly occupied level is at about 3.3 eV above the top of the valence band and well above the  $O_2 \pi^*$  orbitals), much more complex is the answer to the second point. In fact, in order to be transferred to an adsorbed species the excess electrons should be thermally promoted to the conduction band, where they gain mobility. However, the energy levels of  $V_O$  species are quite deep in the gap, and an optical excitation of about 2 eV is required to promote the electrons to the CB, Fig. 13.

A possible tentative explanation for the observed behaviour is that the unknown X center corresponds to electrons trapped in grain boundaries. Recent theoretical<sup>49, 50</sup> and experimental evidences<sup>51</sup> show that indeed these extended defects can accommodate extra electronic charge. A recent light emission and STM study, complemented by EPR spectroscopy, on metal supported MgO ultra thin films has provided evidence on the ability of line defects in trapping electrons. An EPR spectrum of such electrons has been reported which practically coincides with our signal II ( $g = 2.0023$ , symmetric line)<sup>51</sup>. This important correspondence reinforces the hypothesis that the relatively few electrons associated to signal II together with the EPR silent electrons present in the annealed solid are both associated to some particular “pocket” present in line defects or in grain boundaries of the solid. In an ionic oxide like MgO these sites have energy levels high in the gap, so that electrons can easily be excited into the conduction band and transferred to adsorbed species. Other possible kinds of excess electrons, like for instance free carriers in CB, are unlikely, due to the total absence of any effect in the UV-Vis spectra of the reduced material (Fig. 2b). Therefore, no conclusive proof can be provided at this level on the exact nature of the diamagnetic electron traps and of the related paramagnetic variant ( $g=2.0024$ ) even though the

hypothesis on grain boundaries and extended defects assumes a definite strength.

## ACKNOWLEDGMENT

This work has been supported by the CARIPLO Foundation with the Advanced Materials Grant 2009 “Development of second generation photocatalysts for energy and environment” and by the Italian Ministry of University and Research, MIUR, through the “Programs of National Relevance” (PRIN-2009) and the “National Funding for Basic Research” (FIRB) with a project entitled “Oxides at the nanoscale: functionalities and applications” (FIRB RBAP11AYN).

## REFERENCES

1. Ward, D. A.; Ko, E. I. *Chem. Mater.* **1993**, 5, 956.
2. Brown, M.; Primdahl, S.; Mogensen, M. J. *Electrochem. Soc.* **2000**, 147, 475.
3. Tanabe, K. *Mater. Chem. Phys.* **1985**, 13, 347.
4. Yamaguchi, T. *Catal. Today* **1994**, 20, 199.
5. Corma, A. *Chem. Rev.* **1995**, 95, 559.
6. Sayama, K.; Arakawa, H. *J. Phys. Chem.* **1993**, 97, 531.
7. Kohno, Y.; Tanaka, T.; Funabiki, T.; Yoshida, S. *Chem. Commun.* **1997**, 841.
8. Kohno, Y.; Tanaka, T.; Funabiki, T.; Yoshida, S. *J. Chem. Soc., Faraday Trans.* **1998**, 94, 1875.
9. Goff, J. P.; Hayes, W.; Hull, S.; Hutchings, M. T.; Clausen, K. N. *Phys. Rev. B* **1999**, 59, 14202.
10. Catlow, C. R. A.; Chadwick, A. V.; Greaves, G. N.; Moroney, L. M. *J. Am. Ceram. Soc.* **1986**, 69, 272.
11. Ritala, M.; Leskela, M. *Appl. Surf. Sci.* **1994**, 75, 333.
12. Morterra, C.; Giamello, E.; Orio, L.; Volante, M. *J. Phys. Chem.* **1990**, 94, 3111.
13. Giamello, E.; Volante, M.; Fubini, B.; Geobaldo, F.; Morterra, C. *Mater. Chem. Phys.* **1991**, 29, 379.
14. Bedilo, A. F.; Plotnikov, M. A.; Mezentseva, N. V.; Volodin, A. M.; Zhidomirov, G. M.; Rybkin, I. M.; Klabunde, K. J. *Phys. Chem. Chem. Phys.* **2005**, 7, 3059.
15. Frolova, E. V.; Ivanovskaya, M. I. *Mater. Sci. Eng., C* **2006**, 26, 1106.
16. Livraghi, S.; Olivero, F.; Paganini, M. C.; Giamello, E. *J. Phys. Chem. C* **2010**, 114, 18553.
17. Dovesi, R.; Orlando, R.; Civalieri, B.; Roetti, C.; Saunders, V. R.; Zicovich-Wilson, C. M. *Z. Kristallogr.* **2005**, 220, 571.
18. Dovesi, R.; Saunders, V. R.; Roetti, C.; Orlando, R.; Zicovich-Wilson, C. M.; Pascale, F.; Civalieri, B.; Doll, K.; Harrison, N. M.; Bush, I. J.; D'Arco, P.; Llunell, M., *CRYSTALOG User's Manual*; University of Torino: Torino, 2009.
19. Becke, A. D. *J. Chem. Phys.* **1993**, 98, 5648.
20. Lee, C. T.; Yang, W. T.; Parr, R. G. *Phys. Rev. B* **1988**, 37, 785.
21. Gallino, F.; Pacchioni, G.; Di Valentin, C. *J. Chem. Phys.* **2010**, 133.
22. Lutterotti, L.; Bortolotti, M.; Ischia, G.; Lonardelli, I.; Wenk, H. R. *Z. Kristallogr.* **2007**, 125.
23. French, R. H.; Glass, S. J.; Ohuchi, F. S.; Xu, Y. N.; Ching, W. Y. *Phys. Rev. B* **1994**, 49, 5133.
24. Occhiuzzi, M.; Cordischi, D.; Dragone, R. *J. Phys. Chem. B* **2002**, 106, 12464.
25. Volodin, A. M. *Catal. Today* **2000**, 58, 103.
26. Ivanovskaya, M. I.; Frolova, E. V. *Russ. J. Gen. Chem.* **2007**, 77, 524.

27. Zhao, Q.; Wang, X. P.; Cai, T. X. *Appl. Surf. Sci.* **2004**, 225, 7.
28. Calatayud, M.; Markovits, A.; Menetrey, M.; Mguig, B.; Minot, C. *Catal. Today* **2003**, 85, 125.
29. Anpo, M.; Che, M.; Fubini, B.; Garrone, E.; Giamello, E.; Paganini, M. C. *Top. Catal.* **1999**, 8, 189.
30. Purnell, I. J.; Chiesa, M.; Farley, R. D.; Murphy, D. M.; Rowlands, C. C.; Paganini, M. C.; Giamello, E. *Magn. Reson. Chem.* **2002**, 40, 381.
31. Ricci, D.; Di Valentin, C.; Pacchioni, G.; Sushko, P. V.; Shluger, A. L.; Giamello, E. *J. Am. Chem. Soc.* **2003**, 125, 738.
32. Livraghi, S.; Chiesa, M.; Paganini, M. C.; Giamello, E. *J. Phys. Chem. C* **2011**, 115, 25413.
33. Chiesa, M.; Paganini, M. C.; Giamello, E.; Murphy, D. M.; Di Valentin, C.; Pacchioni, G. *Acc. Chem. Res.* **2006**, 39, 861.
34. Chiesa, M.; Giamello, E.; Di Valentin, C.; Pacchioni, G. *Chem. Phys. Lett.* **2005**, 403, 124.
35. Chiesa, M.; Paganini, M. C.; Giamello, E.; Di Valentin, C.; Pacchioni, G. *Chemphyschem* **2006**, 7, 728.
36. Berger, T.; Diwald, O.; Knoezinger, E.; Napoli, F.; Chiesa, M.; Giamello, E. *Chem. Phys.* **2007**, 339, 138.
37. Maurelli, S.; Livraghi, S.; Chiesa, M.; Giamello, E.; Van Doorslaer, S.; Di Valentin, C.; Pacchioni, G. *Inorg. Chem.* **2011**, 50, 2385.
38. Livraghi, S.; Maurelli, S.; Paganini, M. C.; Chiesa, M.; Giamello, E. *Angew. Chem. Int. Ed.* **2011**, 50, 8038.
39. Howe, R. F.; Gratzel, M. *J. Phys. Chem.* **1985**, 89, 4495.
40. Pacchioni, G.; Freund, H. J. *Chem. Rev.*, in press.
41. Ramo, D. M.; Gavartin, J. L.; Shluger, A. L.; Bersuker, G. *Phys. Rev. B* **2007**, 75, 12.
42. McComb, D. W. *Phys. Rev. B* **1996**, 54, 7094.
43. Di Valentin, C.; Pacchioni, G.; Selloni, A. *J. Phys. Chem. C* **2009**, 113, 20543.
44. Shluger, A. L.; Sushko, P. V.; Kantorovich, L. N. *Phys. Rev. B* **1999**, 59, 2417.
45. Sushko, P. V.; Shluger, A. L.; Catlow, C. R. A. *Surf. Sci.* **2000**, 450, 153.
46. Ganduglia-Pirovano, M. V.; Hofmann, A.; Sauer, J. *Surf. Sci. Rep.* **2007**, 62, 219.
47. Ferrari, A. M.; Pacchioni, G. *J. Phys. Chem.* **1995**, 99, 17010.
48. Ramo, D. M.; Sushko, P. V.; Gavartin, J. L.; Shluger, A. L. *Phys. Rev. B* **2008**, 78.
49. McKenna, K. P.; Shluger, A. L. *Phys. Rev. B* **2009**, 79.
50. Wolf, M. J.; McKenna, K. P.; Shluger, A. L. *J. Phys. Chem. C* **2012**, 116, 25888.
51. Benia, H.-M.; Myrach, P.; Gonchar, A.; Risse, T.; Nilus, N.; Freund, H.-J. *Phys. Rev. B* **2010**, 81.

